**CONTRIBUTIONS TO MODERN AND APPLIED PHYSICS**
Vol. 1, No. 1, 2024, 1–8
Received: 15/03/2024, Accept: 04/04/2024, Published: 10/04/2024
DOI: https://doi.org/10.33790/cmap1100101

# Operation of BGO with SiPM Readout at Dry Ice and Liquid Nitrogen Temperatures

**Keyu Ding, Jing Liu***
Department of Physics, University of South Dakota, 414 East Clark Street, Vermillion, SD 57069, USA

Corresponding Author: Jing Liu, Department of Physics, University of South Dakota, 414 East Clark Street, Vermillion, SD 57069, USA.

## ABSTRACT

**The light yield and decay constant of BGO were measured at both dry ice and liquid nitrogen temperatures using two SiPMs directly coupled to a $6 \times 6 \times 6$ cm$^2$ cubic BGO crystal. With the measured light yield (5.2±0.3 PE/keV at dry ice temperature and 10.5±0.4 PE/keV at liquid nitrogen temperature) and decay constants, potential applications of BGO in ToF-PET and SPECT were discussed.**

**Keywords:** ***BGO, SiPM, PET, SPECT, light yield, scintillation, Compton suppression, cryogenic operation***



## 1. INTRODUCTION

The Bismuth Germanate ($Bi_4Ge_3O_{12}$, BGO in short) scintillating crystal boasts a few properties that make it great for radiation detection in general. First, it is not hygroscopic, not fragile, hence is easy to handle. Second, it can be obtained at a reasonable price and is among the cost-effective solutions for many applications. Third, the high density (7.13 g/cm$^3$) and the effective atomic number (74) of BGO make it very effective in absorbing $\gamma$-ray radiation [1], such as the 511 keV $\gamma$-ray utilized in positron emission tomography (PET) [2-4], the 141 keV $\gamma$-ray utilized in single photon emission computerized tomography (SPECT) [5], or Compton-scattered $\gamma$-rays from more sensitive detectors, such as high-purity germanium detectors [6, 7]. Finally, BGO also finds its applications in fundamental science research. The high atomic number of Bi leads to its high cross-sections for neutrinos and dark matter particles coherent scatterings, which is a desirable property in detecting these rare physics phenomena [8].

However, the intrinsic light yield ($Y$) of BGO is not particularly high, only about 15–20% of that of NaI(Tl). It is also a relatively slow scintillator, the decay time ($\tau_{\text{decay}}$) is about 300 ns at room temperature. $\sqrt{Y/\tau_{\text{decay}}}$ is a commonly used figure-of-merit (FOM) to assess how well a scintillator can provide time information in modern PET that utilizes the time-of-flight (ToF) technique to improve image resolution [2]. According to this FOM, Lutetium Oxyorthosilicate (Lu2SiO5:Ce, LSO in short) and Lutetium-Yttrium Oxyorthosilicate (LYSO) are about 10 times better than BGO in the application of ToF-PET [2], as they possess about three times higher light yields and about 10 times shorter decay times. However, L(Y)SO suffers from intrinsic radiation and is much more costly than BGO. If there is some way to modify the light yield and decay time of BGO, we may find a niche for BGO in medical imaging applications.

It has been observed that the light yield of BGO increases as the temperature goes down [9, 10]. At liquid nitrogen temperature, its light yield is about five times higher than that at room temperature (left in Fig. 1). Unfortunately, its decay time also increases as the temperature goes down [10]. At liquid nitrogen temperature, the larger decay constant is about thirty times longer than that at room temperature (right in Fig. 1). It is hence of interest to find a temperature in between, where the light yield is already significantly higher than that at room temperature, but the decay time has not yet become too long. The dry ice temperature, 194.7 K, which is convenient to obtain, seems to be a reasonable choice, where the light yield is already 3 times higher than that at room temperature while the decay constant is only twice higher than that at room temperature. Properties at 77 K are still worth probing as the light yield doesn't change much anymore below 77 K and it is easy to get to this temperature using liquid nitrogen. With a cryo-cooler, other temperatures can also be used. But practically, a cryo-cooler is much more expensive than liquid nitrogen and dry ice.

Cherenkov emission is much faster than scintillation. There is an increasing interest in the ToF-PET community to utilize it for better timing resolution (See Ref. [3] and references therein). A photo-electron created by a 511 keV gamma-ray in BGO can create on average $\sim$ 20 Cherenkov photons in the range of 305–750 nm in about 20 picoseconds (ps), about twice more and faster than that of LSO [3]. If one uses the Cherenkov emission in BGO for timing information and scintillation for energy information, the prolonged decay time of BGO after cooling becomes less a concern.

The readout of light signals at cryogenic temperatures necessitates the use of cryogenic light sensors. In recent years, cryogenic-compatible light sensors have emerged, with silicon photomultiplier (SiPM) being one of them. SiPMs offer several

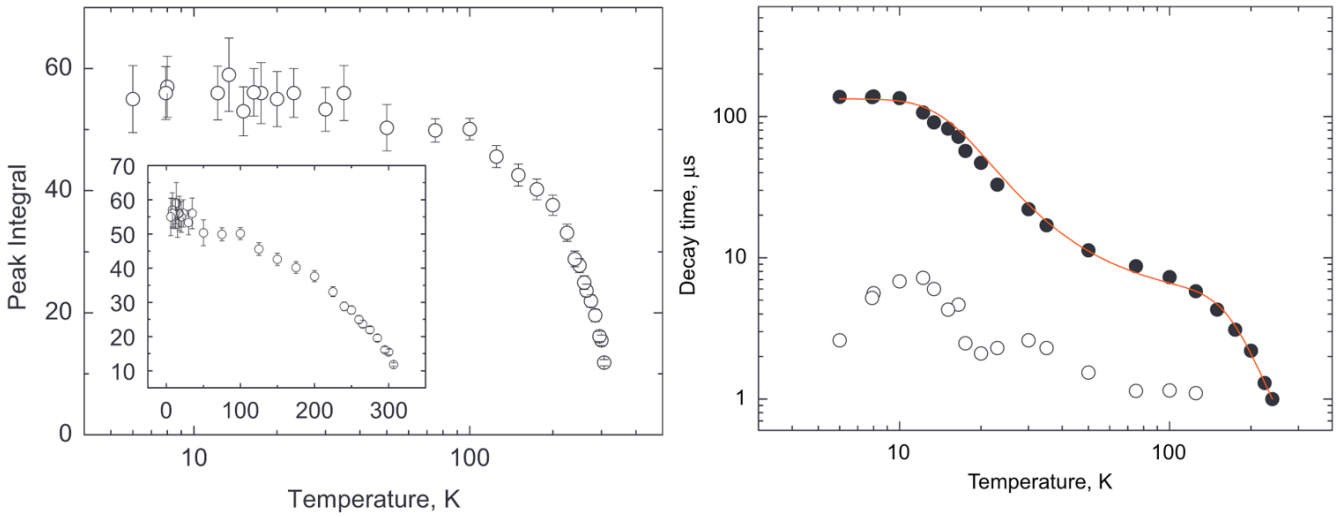


**Figure 1** Scintillation light yield (left) and decay constants (right) of BGO at various temperatures. Taken from Ref. [10].

advantages over photomultiplier tubes (PMTs), including higher photon detection efficiency (PDE), absence of high voltage requirements, and reduced bulkiness. One drawback of SiPMs compared to PMTs is that they have a much higher dark count rate (DCR) than PMTs at room temperature. Fortunately, the rate drops quickly as the temperature goes down. Therefore, exploring the combination of BGO and SiPM at cryogenic temperatures is a worthwhile endeavor. The proposed combination also possesses a few advantages over the traditional NaI(Tl) + PMT arrays in a typical SPECT system. First, as BGO is almost twice denser than NaI(Tl), it can be made twice thinner (about 0.3 cm) than the latter while maintaining the same absorption efficiency for 141 keV $\gamma$-rays. This will dramatically increase the camera's spatial resolution since less photons can be spread out to photon sensors far away [11-14]. Second, it possesses all advantages of SiPMs over PMTs as mentioned previously. The light yield of BGO at room temperature is only about 25% of that of NaI(Tl). However, this may be overcome by the cryogenic operation of BGO.

This paper reports measurements of light yields and decay constants from a cubic BGO crystal directly coupled with two SensL SiPMs at both liquid nitrogen and dry ice temperatures. The 59.5 keV $\gamma$-ray peak from a $^{241}$Am source, the 30.85 keV $X$-ray peak, and the 81 keV $\gamma$-ray peak from a $^{133}$Ba source were used for the measurements. To the authors' knowledge, such an operation has not yet been reported in the literature.

## 2. Experimental setup

The experimental setup is shown in Fig. 2. The $6\times6\times6$ mm$^3$ cubic BGO crystal was purchased from https://www.x-zlab.com. To prevent any light leakage, the side surfaces of the crystal were wrapped with multiple layers of Teflon tape. The Teflon wrapping also randomizes the reflection direction to avoid trapping a photon in the crystal due to total internal reflection. Side surfaces of the crystal were unpolished for the same reason. The top and bottom surfaces in direct contact with the SiPMs were also unpolished. Light loss is likely to happen in such an interface. There is room for improvement. We are in the process of designing new experiments with various surface conditions to investigate in detail how surface treatment affects the light collection efficiency. The result will be published in a separate manuscript. Two MicroFJ-SMTPA-60035 SiPMs from SensL [15] were directly coupled to the top and bottom surfaces of the crystal without optical grease, which may degrade at cryogenic temperature. A constant bias voltage of 29 V was applied to both sensors. The two sensors were directly soldered onto two passive boards. Detailed circuit diagrams and PCB layouts can be found in Ref. [16]. To establish optimal optical contact without the use of optical grease, we secured the PCBs against the crystal's end surfaces using springs. Two radioactive sources were used separately. An $^{241}$Am source was positioned by the side of the crystal, as shown in Fig. 2. A $^{133}$Ba source was placed at the bottom of the cryostat, slightly further away from the crystal compared to $^{241}$Am.

Given BGO's non-hygroscopic nature, setups were assembled in a standard room environment. The SiPM-BGO assembly was then lowered into a stainless steel chamber through its top opening, as illustrated in the schematic in the middle of Fig. 2. The chamber had an inner diameter of approximately 10 cm and a length of 50 cm. Both ends of the chamber were hermetically sealed under vacuum conditions, using two 6-inch ConFlat (CF) flanges. The bottom flange was blank and affixed to the chamber with a copper gasket in between. For ease of access during multiple operations, the top flange was attached to the chamber with a fluorocarbon CF gasket. The top flange featured vacuum-welded connections for five BNC, two SHV, one 19-pin electronic feedthrough, and two 1/4-inch VCR connectors.

Once all the cables were securely positioned within the chamber, the top flange was sealed. The chamber was subsequently evacuated using a Pfeiffer Vacuum HiCube 80 Eco pump to reach a vacuum level of approximately $1.0\times10^{-4}$ mbar. Subsequently, it was pressurized with dry nitrogen gas to approximately 1.8 Kgf/cm$^2$ and then carefully placed into an open

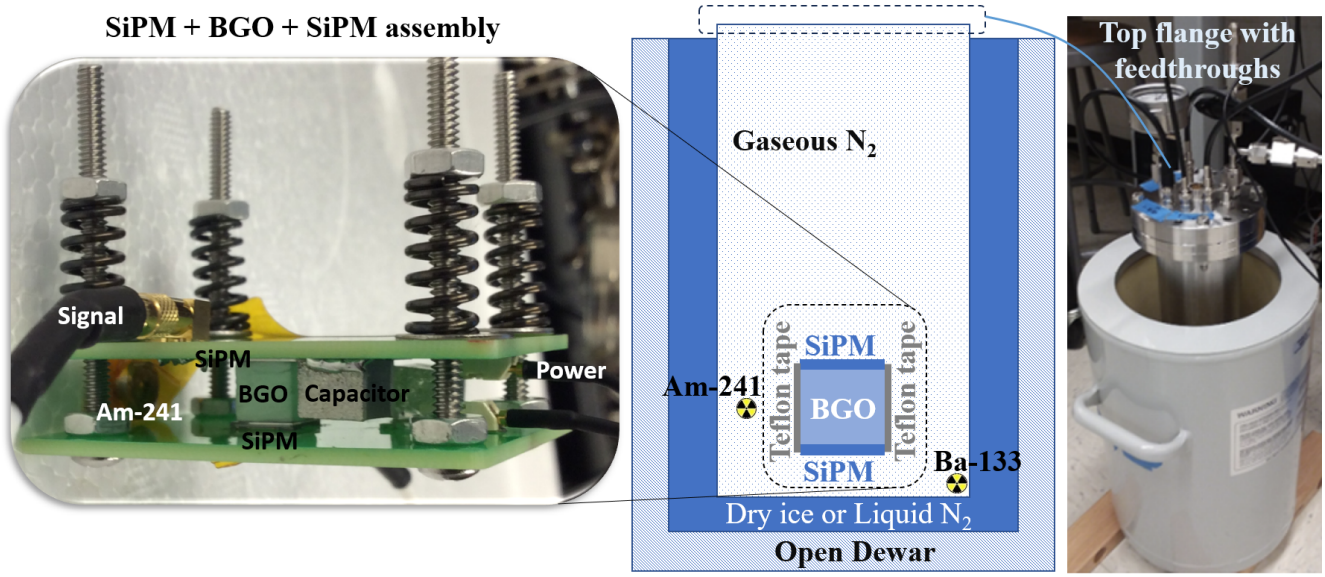


**Figure 2** A picture and a sketch of experimental setups.

$LN_2$ dewar. The dewar was subsequently filled with either $LN_2$ or dry ice to cool both the chamber and its contents.

A few Heraeus C 220 platinum resistance temperature sensors were employed to monitor the cooling process effectively. These sensors were affixed to the side surface of the crystal, the bottom flange, and the top flange to obtain the temperature profile of the long chamber. For data acquisition from the sensors, we utilized a Raspberry Pi 2 computer running custom software [17]. The cooling process took about half an hour due to the small size of the crystal. Most measurements, however, were conducted after approximately two hours of waiting to ensure the system reached thermal equilibrium. Notably, the temperature of the crystal remained consistent before and after each measurement.

The passive boards were powered by a RIGOL DP821A DC power supply [18]. A voltage of 29 V was applied to the SiPMs. According to their manuals, the photon detection efficiency (PDE) at this voltage is $\sim 50\%$ for MicroFJ-SMTPA-60035 at 420 nm and room temperature. Signals were further amplified using a Phillips Scientific Quad Bipolar Amplifier Model 771, featuring four channels, each with a gain of ten. By chaining two channels together, a maximum gain of $10\times10$ was employed. The amplified pulses were subsequently routed into a CAEN DT5720 waveform digitizer, with a 250 MHz sampling rate, a dynamic range of 2 V, and a 12-bit resolution. Data recording was carried out using WaveDump [19], a free software tool provided by CAEN. The recorded binary data files were later converted to CERN ROOT files for analysis [20].

## 3. Single photo-electron response

Single photo-electron (SPE) responses of individual channels were investigated by analyzing waveform data triggered by dark counts. To filter out noisy events while still capturing the majority of SPE pulses, a threshold of 20 ADC counts was set. Prior to the rising edge of the pulse that triggered the digitizer, some pre-traces (100 samples) were preserved to calculate the baseline value of a waveform. This baseline value was subsequently subtracted from each sample of the waveform. The left plot in Fig. 3 shows a random single PE waveform overlaid with the averaged SPE waveform. The averaged SPE waveform was generated by adding 1000 SPE pulses together and then dividing the resulting summed waveform by 1000. Random electronic noise was canceled out in the averaged SPE waveform and a stable baseline was revealed. The integration window, [250, 600] ns, was determined based on the averaged SPE waveform.

The right plot in Fig. 3 shows the distribution of integrated pulse areas. Individual photo-electron (PE) peaks are clearly distinguishable. The ninth peak was fitted using a Gaussian function to obtain its mean value. The same operations were performed for all other peaks. The mean of an SPE, $\text{mean}_{1\text{PE}}$, is defined as the Gaussian mean divided by the number of PEs, $n$. For instance, the $\text{mean}_{\text{SPE}}$ calculated using the ninth peak is $26971/9 = 2996$ ADC counts·ns. The discrepancy of $\text{mean}_{\text{SPE}}$ from different peaks is within 3%. The same measurement was repeated multiple times before and after an energy calibration measurement. The discrepancy of $\text{mean}_{\text{SPE}}$ in multiple measurements was within 6%. which was taken as the uncertainty of $\text{mean}_{\text{SPE}}$.

To summarize, $\text{means}_{\text{SPE}}$ obtained from the top SiPM in the dry ice temperature runs was 2996 ADC counts·ns, and 2972 ADC counts·ns for the bottom SiPM. In general, the breakdown voltage, $V_{\text{bd}}$, of a SiPM decreases as the temperature goes down. As we kept the same bias voltage, $V_{\text{bias}}$, for all measurements, the over voltage, $V_{\text{over}} = V_{\text{bias}} - V_{\text{bd}}$, was higher at lower temperatures. This led to an increased gains of both SiPMs at liquid nitrogen temperature. $\text{Means}_{\text{SPE}}$ from the top SiPM in the liquid nitrogen temperature runs increased to 3716 ADC counts·ns, and for the bottom SiPM, it increased to 3713 ADC counts·ns.

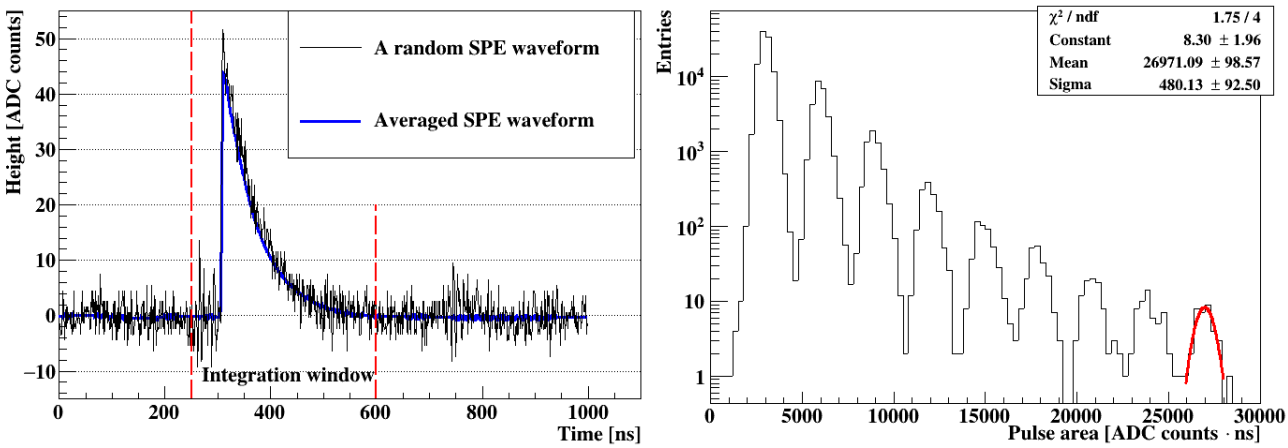


**Figure 3** Left: A random single photon-electron (SPE) waveform and the averaged SPE waveform meaasured with the top SiPM at 195 K. Right: SPE distribution in logarithm scale with a Gaussian fitted to the last peak. Note: SPE responses from other temperatures and the other SiPM are very similar.

## 4. Energy calibration

The energy calibration was performed using $X$-rays and $\gamma$-rays from the $^{241}$Am and the $^{133}$Ba radioactive sources individually. The digitizer was triggered when the heights of pulses from both SiPMs were more than 100 ADC counts (∼2 to 3 PEs). Pulses induced by radiation from the source were well above the threshold. The coincident trigger rate was around 240 Hz at dry ice temperature.

Several waveform selection criteria were applied. First, the room mean square (RMS) of the first 100 baseline samples was calculated for each waveform. If it was more than 3.5 ADC counts, that waveform was rejected. Second, waveforms that went beyond the digitizer's dynamic range (region ① in Fig. 4) were rejected. Third, waveforms that had pre-pulses above the threshold (region ② in fig. 4) was removed. Only waveforms triggered within [1450, 1460] ns were selected.

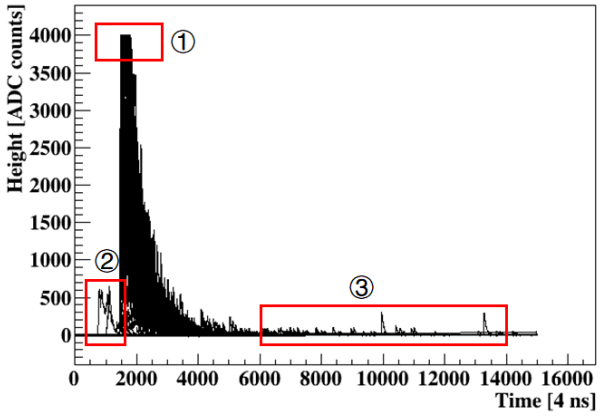


**Figure 4** One hundred random waveforms from the top SiPM at dry ice temperature.

At dry ice temperature, integration in [1400, 6000] ns was performed for waveforms passing all criteria. The integration has a unit of ADC counts·ns. The resulting energy spectra of $^{241}$Am and $^{133}$Ba are presented in Fig. 5. It seems from Fig. 4 that tails of some pulses go beyond 6000 ns into region ③. However, the averaged waveform calculated using the 81 keV peak (right most peak in Fig. 5) shown in the left plot in Fig. 6 in Section 6 justifies the range of integration. At liquid nitrogen temperature, light pulses were significantly prolonged as shown in the right plot in Fig. 6. The corresponding integration range is [1400, 12000] ns.

## 5. Light yield

The integrated pulse areas, $A$, of the selected waveforms follow the Gaussian distribution as shown in Fig. 5. In the left plot, a Gaussian was fitted to the 59.5 keV peak from $^{241}$Am. In the right plot, a straight line was used to characterize the background, while two combined Gaussian functions were used to fit the 30.85 keV and 81 keV peaks from $^{133}$Ba. The fitting results were summarized in Table 1–4.

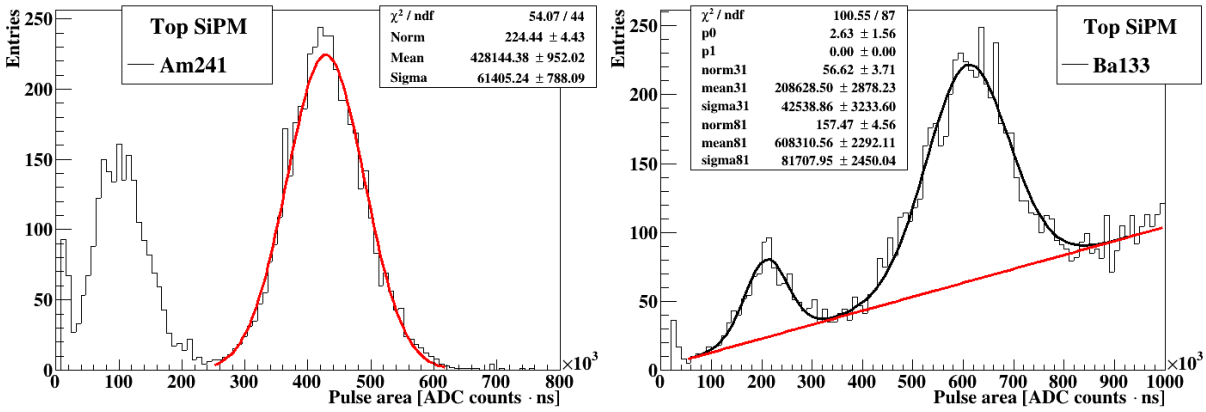


**Figure 5** Energy spectra of $^{241}$Am (left) and $^{133}$Ba (right) observed from the top SiPM at dry ice temperature. Gaussian fitting were performed for three peaks (from left to right: 59.5 keV from $^{241}$Am, 30.85 and 81 keV from $^{133}$Ba).

The fitted means of $A$ corresponding to the 30.85 keV, 59.5 keV and 81 keV peaks in the $^{241}$Am and $^{133}$Ba spectra in the unit of ADC counts·ns were converted to the number of PE using the following formula:

$$\text{number of PEs} = \frac{\text{Mean (A) [ADC counts} \cdot \text{ns]}}{\text{mean}_{\text{SPE}}}, \tag{1}$$

and the light yield was calculated using the data in Table 1–4 and the following formula:

$$\text{light yield [PE/keV}_{\text{ee}}\text{]} = \frac{\text{number of PEs}}{\text{Energy [keV}_{\text{ee}}\text{]}}. \tag{2}$$

Combining the results from both the top and the bottom SiPM, a light yield of $5.2 \pm 0.3$ PE/keV$_{\text{ee}}$ at 81 keV was observed at dry ice temperature, and $10.5 \pm 0.4$ PE/keV$_{\text{ee}}$ was observed at liquid nitrogen temperature. Yields measured at different energy points are consistent with each other within the uncertainty. However, there is a hint that the yield decreases slightly as the energy goes down. If this is true, it could be explained by either the observed non-linear energy response of BGO [21, 22], or the fact that lower energy photons cannot penetrate deep into the crystal, they produce scintillation light much closer to the rough surface of the crystal, and the produced scintillation light has higher chance to be trapped or absorbed by surface defects.

**Table 1** Light yield obtained at dry ice temperature from the top SiPM.

| Type of radiation | Source | Energy [keV] | Mean (A) [ADC·ns] | Sigma [ADC·ns] | FWHM % | Light yield [PE/keV$_{\text{ee}}$] | Uncertainty [PE/keV$_{\text{ee}}$] |
|---|---|---|---|---|---|---|---|
| $\gamma$-ray | Ba-133 | 30.85 | 208629 | 42539 | 48 | 2.3 | $\pm$ 0.1 |
| $\gamma$-ray | Am-241 | 59.5 | 428144 | 61405 | 34 | 2.4 | $\pm$ 0.1 |
| $\gamma$-ray | Ba-133 | 81 | 608311 | 81708 | 32 | 2.5 | $\pm$ 0.2 |

**Table 2** Light yield obtained at dry ice temperature from the bottom SiPM.

| Type of radiation | Source | Energy [keV] | Mean (A) [ADC·ns] | Sigma [ADC·ns] | FWHM % | Light yield [PE/keV$_{\text{ee}}$] | Uncertainty [PE/keV$_{\text{ee}}$] |
|---|---|---|---|---|---|---|---|
| $\gamma$-ray | Ba-133 | 30.85 | 231940 | 45189 | 46 | 2.5 | $\pm$ 0.1 |
| $\gamma$-ray | Am-241 | 59.5 | 427219 | 62083 | 34 | 2.4 | $\pm$ 0.1 |
| $\gamma$-ray | Ba-133 | 81 | 657506 | 91739 | 33 | 2.7 | $\pm$ 0.2 |

## 6. Decay constant

The decay constants of BGO at dry ice (195 K) and liquid nitrogen (77 K) temperatures were obtained by fitting exponential functions to the averaged waveforms in the 81 keV peak. The process of generating an averaged waveform is explained using the data from the top SiPM at 195 K. First, waveforms that have a pulse area in [550,000, 650,000] ADC counts·ns were selected (less than $\pm 1\sigma$ around the mean of the 81 keV peak shown in Fig. 5). Second, the selected waveforms were summed. Third, the summed waveform was divided by the total number of selected waveforms to obtained the averaged waveform, which is shown in the left plot in Fig. 6. The averaged waveform at liquid nitrogen temperature is shown in the right plot.

**Table 3** Light yield obtained at liquid nitrogen temperature from the top SiPM.

| Type of radiation | Source | Energy [keV] | Mean (A) [ADC·ns] | Sigma [ADC·ns] | FWHM % | Light yield [PE/keV$_{ee}$] | Uncertainty [PE/keV$_{ee}$] |
|---|---|---|---|---|---|---|---|
| $\gamma$-ray | Ba-133 | 30.85 | 477785 | 131485 | 65 | 4.2 | $\pm$ 0.2 |
| $\gamma$-ray | Am-241 | 59.5 | 1095347 | 166360 | 36 | 5.0 | $\pm$ 0.3 |
| $\gamma$-ray | Ba-133 | 81 | 1515401 | 195567 | 30 | 5.0 | $\pm$ 0.3 |

**Table 4** Light yield obtained at liquid nitrogen temperature from the bottom SiPM.

| Type of radiation | Source | Energy [keV] | Mean (A) [ADC·ns] | Sigma [ADC·ns] | FWHM % | Light yield [PE/keV$_{ee}$] | Uncertainty [PE/keV$_{ee}$] |
|---|---|---|---|---|---|---|---|
| $\gamma$-ray | Ba-133 | 30.85 | 549115 | 117970 | 51 | 4.8 | $\pm$ 0.3 |
| $\gamma$-ray | Am-241 | 59.5 | 1166037 | 173975 | 35 | 5.3 | $\pm$ 0.3 |
| $\gamma$-ray | Ba-133 | 81 | 1655799 | 222286 | 32 | 5.5 | $\pm$ 0.3 |

As mentioned in the introduction, the decay time of scintillation emission in BGO increases dramatically as the temperature goes down. This demands different ranges for analysis at different temperatures. At dry ice temperature, the selected range for analysis is [1600, 5000]$\times$4 ns, while at liquid nitrogen temperature, the selected range is [1600, 12000]$\times$4 ns. Note that at dry ice temperature a single exponential decay function can describe the averaged waveform in the analysis range very well, while at liquid nitrogen temperature a fast and a slow exponential decay must be used to describe the average waveform in the selected range. The corresponding fitting functions and results are shown in Fig. 6. A single decay constant, $442 \times 4 = 1768$ ns, was observed at 195 K. A fast decay constant, $748 \times 4 = 2992$ ns, and a slow decay constant, $2253 \times 4 = 9012$ ns, were observed at 77 K. The observed upward trend in the decay constant with the decreasing temperature in BGO is consistent with the literature [10].

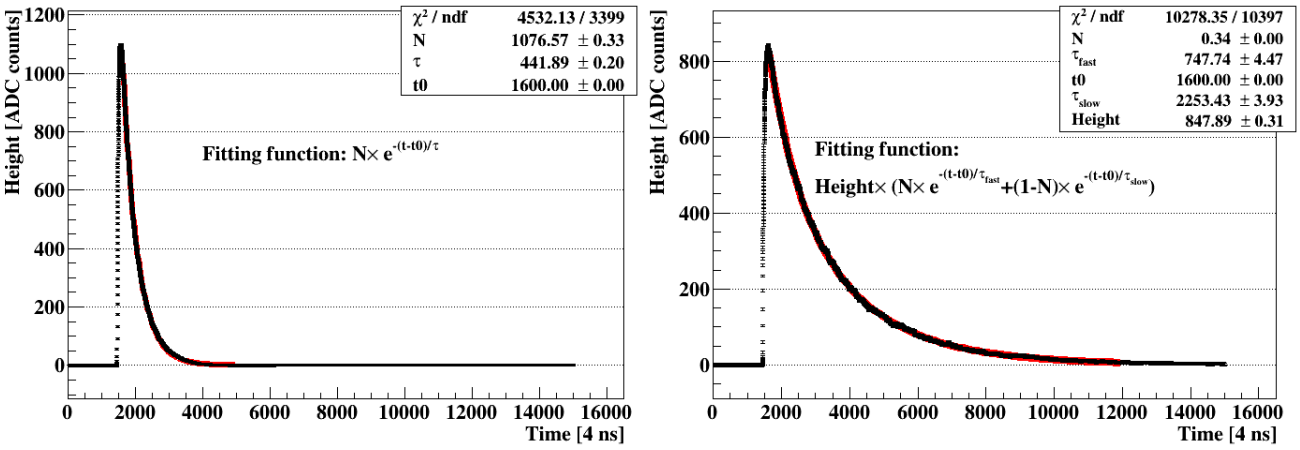


**Figure 6** Averaged 81 keV waveforms at dry ice temperature (left) and liquid nitrogen temperature (right).

# 7. Discussion

Using the measured light yields and decay constants, FOM of BGO for ToF-PET can be calculated. Note that the light yield defined in Section 5 is the yield of the whole detector system, not the intrinsic yield of the crystal. Since the latter is used to calculate the FOM in the literature [2], the following equation was used to convert the system yield to the intrinsic yield for easy comparison:

$$\text{intrinsic light yield} = \text{(system light yield)/(PDE of SiPM)/(light collection efficiency)/(cross talk correction)} \quad (3)$$

According to the SiPM manual from the manufacturer [23], the PDE at 480 nm (peak scintillation wavelengh of BGO) is about 45%. The light collection efficiency from our Geant4 optical simulation is about 80%. Optical cross talks between neighboring cells within a SiPM or between two face-to-face SiPMs increases the number of observed photon-electrons artificially [24-27]. This effect must be corrected. According to Ref. [27], the breakdown voltage of the SiPMs used in this measurement is about 21 V. Biased at 29 V, both SiPMs were operated with a breakdown voltage of about 8 V. The number of detected photoelectrons should be doubled due to cross talk [26]. The cross talk correction should hence be around 200%. The intrinsic light yield is then 5.2/45%/80%/200%$\sim$7 photons/keV (or 7,000 photons/MeV) at dry ice temperature, and 10.3/45%/80%/200%$\sim$14.5 photons/keV (or 14,500 photons/MeV) at liquid nitrogen temperature. The FOM is

then $\sqrt{7000/1768} = 2.0/\sqrt{\text{MeV}\cdot\text{ns}}$ at dry ice temperature, and $\sqrt{14500/2992} = 2.2/\sqrt{\text{MeV}\cdot\text{ns}}$ (fast decay constant), $\sqrt{14500/9012} = 1.3/\sqrt{\text{MeV}\cdot\text{ns}}$ (slow decay constant) at liquid nitrogen temperature. They are about 10 times smaller than the typical FOM for LYSO/LSO crystals (27–32 $/\sqrt{\text{MeV}\cdot\text{ns}}$ [2]). The light yield of cooled BGO is compatible to that of LYSO/LSO. However, the significantly prolonged decay constant of cooled BGO cancels out all the benefit from the increased light yield.

One potential solution is to use the Cherenkov radiation emitted by photo-electrons created by incident $\gamma$-rays to obtain ToF and to use the scintillation light for energy information. The Cherenkov radiation in BGO is emitted within 30 ps [3]. The FOM calculated using this number is $\sqrt{14500/0.03} = 695/\sqrt{\text{MeV}\cdot\text{ns}}$, more than 20 times better than that of LYSO/LSO. Cherenkov photons are emitted from electrons moving fast than the speed of light in BGO. The differential Cherenkov photon yield can be calculated based on the Frank-Tamm formula [28],

$$\frac{\mathrm{d}N^2}{\mathrm{d}x\mathrm{d}\lambda} = \frac{2\pi\alpha}{\lambda^2}\left(1 - \frac{1}{n^2(\lambda)\beta^2}\right), \tag{4}$$

where, $x$ is the electron track length, $\lambda$ is the wavelength of the emitted photons, both have the unit of meter, $\alpha \approx 1/137$ is the fine-structure constant, $\beta = v/c$, and $v$ is the speed of electron, $n$ is the refraction index of the medium, which is a function of $\lambda$. It shows in the formula that the larger the refractive index $n$ is, the more Cherenkov photons can be emitted. The refractive index of BGO is 2.39 at 310 nm and 2.2 at 420 nm, much higher than LSO, which is 1.83 at 420 nm. The Cherenkov light yield for 511 keV photons commonly used in a PET is about 20 photons (305–750 nm) for BGO and only 9 photons (390–750 nm) for LSO [3]. Some experimental investigation has shown the possibility to detect Cherenkov light in BGO [3]. The authors plan to try it with cooled SiPMs and that effort will be covered in a separate publication.

The combination of cooled BGO + SiPM light readout also exhibits some great properties as the Anger Camera for a SPECT system, such as a light yield that is compatible to that of NaI(Tl) and a better spatial resolution, etc. The prolonged decay time is less a concern in a SPECT system as the time information is not utilized there.

# 8. Conclusion

The light yield and decay constant of BGO were measured at both dry ice and liquid nitrogen temperatures using two SiPMs directly coupled to a $6 \times 6 \times 6$ cm$^2$ cubic BGO crystal. With the measured light yield (5.2$\pm$0.3 PE/keV at dry ice temperature and 10.5 $\pm$ 0.4 PE/keV at liquid nitrogen temperature) and decay constants, potential applications of BGO in ToF-PET and SPECT were discussed. The increased light yield is very beneficial for both applications. The prolonged decay time is less a concern in SPECT and may be overcome by using Cheronkov radiation instead in a ToF-PET system.

# Acknowledgements

This work is supported by the Department of Energy (DOE), USA, award DE-SC0022167. Computations supporting this project were performed on High Performance Computing systems at the University of South Dakota, funded by NSF award OAC-1626516.

# Conflict of Interest

The authors have no conflict of interest

# References

[1] MELCHER C.L (2000). Scintillation Crystals for PET. *Journal of Nuclear Medicine 41, 1051–1055. Publisher: Society of Nuclear Medicine 226 Section: Continuing Education.*

*[2]* SCHAART, D.R *(*2021*). Physics and technology of time-of-flight PET detectors. Physics in Medicine and Biology, 66, 09TR01.*

*[3]* BRUNNER, S.E*,* SCHAART, D.R *(*2017*). BGO as a hybrid scintillator / Cherenkov radiator for cost-effective time-of-flight PET. Physics in Medicine and Biology, 62, 4421.*

*[4]* KWON, S. I*,* GOLA, A*,* FERRI, A*,* PIEMONTE, C*,* CHERRY, S.R *(*2016*). Bismuth germanate coupled to near ultraviolet silicon photomultipliers for 231 time-of-flight PET. Physics in Medicine and Biology, 61, L38.*

*[5]* PETERSON, T.E*,* FURENLID, L.R *(*2011*). SPECT detectors: the Anger Camera and beyond. Physics in medicine and biology, 56, R145–R182.*

*[6]* WEBER, M.J*,* MONCHAMP, R.R *(*1973*). Luminescence of Bi4 Ge3 O12 : Spectral and decay properties. Journal of Applied Physics, 44, 5495–5499.*

*[7]* DE, VOIGT, BACELAR, J.C*,* MICEK, S.L*,*SCHOTANUS, P*,* VERHOEF, B.A.W*,* WINTRAECKEN, Y.J.E*,* VERMEULEN, P.A *(*1995*). novel compact Ge-BGO Compton-suppression spectrometer. Nuclear Instruments and Methods in Physics Research Section A: Accelerators, Spectrometers, Detectors and Associated Equipment, 356, 362–375.*

[8] ORTIGOZA, Y. *BGO Scintillating Bolometer: Its application in dark matter experiments. http://taup2009.lngs.infn.it/slides/jul3/ortigoza.pdf.*

[9] *BGO — Scintillation Crystal. https://www.x-zlab.com/product/bgo-scintillation-crystal/*

[10] GIRONNET, J. *(*2008*). Scintillation studies of Bi4Ge3O12 (BGO) down to a temperature of 6 K. Nuclear Instruments and Methods in Physics Research Section A: Accelerators, Spectrometers, Detectors and Associated Equipment, 594, 358–361.*

[11] MADSEN, M.T. *(*2007*). Recent Advances in SPECT Imaging. Journal of Nuclear Medicine, 48, 661–673.*

[12] PETERSON, T.E, FURENLID, L.R *(*2011*). SPECT detectors: the Anger Camera and beyond. Phys. Med. Biol, 56, R145–R182.*

[13] RIT, P *(*2022*). Recent Developments in SPECT/CT. Seminars in Nuclear Medicine, 52, 276–285.*

[14] MASSARI, R, MOK, G.S.P *(*2023*). Editorial: New trends in single photon emission computed tomography (SPECT). Front. Med, 10.*

[15] $MicroFJ - SMTPA -$ 60035*. https://www.mouser.com/datasheet/2/308/1/MICROJ_SERIES_D-1489647.pdf.*

[16] DING, K, LIU, J, YANG, Y, CHERNYAK, D. *(*2022*). First operation of undoped CsI directly coupled with SiPMs at 77 K. Eur. Phys. J. C, 82, 344.*

[17] MAMMO, J. *(*2018*). Josephss/CraViS; https://github.com/Josephss/CraViS*

[18] *DP800 High Performance Linear DC Power Supplies — RIGOL. https://www.rigolna.com/products/dc-power-loads/dp800/.*

[19] *WaveDump - CAEN Digitizer readout application. https://www.caen.it/products/caen-wavedump/*

[20] LIU, J. *(*2021*). jintonic/toward. 2021; https://github.com/jintonic/toward*

[21] YAWAI, N, CHEWPRADITKUL, W, WANARAK, C, NIKL, M, RATANATONGCHAI, W *(*2014*). Intrinsic light yield and light loss coefficient of Bi4Ge3O12 single crystals. Optical Materials, 36, 2030–2033.*

[22] MOSZYNSKI, M, BALCERZYK, M, CZARNACKI, W, KAPUSTA, M, KLAMRA, W, SYNTFELD, A, SZAWLOWSKI, M *(*2004*). Intrinsic energy resolution and light yield nonproportionality of BGO. IEEE Transactions on Nuclear Science, 51, 1074–1079.*

[23] *Onsemi Photodetectors. https://www.onsemi.com/products/sensors/photodetectors-sipm-spad.*

[24] MOSZYNSKI, M, BALCERZYK, M, CZARNACKI, W, WANG, L, LI, G.D, YU, Z.Y, LIANG, X.H, WANG, T.A, LIU, F, SUN, X.L, GUO, C, ZHANG, X *(*2022*). Reactor neutrino physics potentials of cryogenic pure-CsI crystal; https://arxiv.org/abs/2212.11515.*

[25] KIM, W, LEE, H, KIM, K, KO, Y, JEON, J, KIM, H, LEE, H *(*2023*). Scintillation characteristics of an undoped CsI crystal at low-temperature for dark matter search. 2023; https://arxiv.org/abs/2312.07957.*

[26] WANG, L, LEI, Y, WANG, T.A, GUO, C, ; ZHAO, K.K, LIANG, X.H, LIU, J.C, YANG, C.G, WANG, S.B, CHEN, Y.D *(*2023*). Developing a single-phase liquid argon detector with SiPM readout. The European Physical Journal Plus, 138, 629.*

[27] WANG, T.A, GUO, C, LIANG, X.H, WANG, L, ; GUAN, M.Y, YANG, C.G, LIU, J.C, LIN, F.Y. *(*2023*). Characterization of two SiPM arrays from Hamamatsu and Onsemi for liquid argon detector. Nuclear Instruments and Methods in Physics Research Section A: Accelerators, Spectrometers, Detectors and Associated Equipment, 1053, 168359.*

[28] FRANK, I.M, TAMM, I.E *(*1937*). Coherent radiation of fast electrons in a medium. Dokl. Akad. Nauk SSSR, 14, 109.*